44th Aerospace Sciences Meeting and Exhibit, Jan.9-12 2006, Reno, NV

Large Eddy Simulation of Film-Cooling Above the Flat Surface with a Large Plenum and Short Exit Holes

Ioulia V. Iourokina* and Sanjiva K. Lele†

Stanford University, Stanford, CA, 94305

Large Eddy Simulation of a realistic film-cooling configuration is performed, consisting of a large plenum feeding a periodic array of short film-cooling holes with length to diameter ratio $L/d = 3.5$. Film-cooling jets are issued at 35 degrees into the turbulent crossflow boundary layer above the flat surface. Details of the flowfield inside the film-cooling hole as well as above the cooled surface are analyzed. Separation is found inside the hole caused by the sharp turning of the flow exiting the plenum. Vortical structures of inclined jet in a crossflow are observed and compared to that found in normals jets. The effect of crossflow fluid entrainment beneath the jet by the low pressure zone is demonstrated and its connection to the film-cooling effectiveness is discussed. Time-averaged velocity field and turbulence statistics are compared to the available experimental data.

I. Introduction

The first stage of the turbine blade experiences a harsh thermal environment. The flows exiting the combustion chamber is at a high temperatures exceeding the melting point of the turbine blade material and is highly turbulent. In order to avoid the detrimental effect of contact between hot gases and blade surface, cooling measures are employed, film-cooling being one of them. However, since film-cooling implies taking some gas out of the compressor, an efficient compromise must be found between the overall engine performance and film-cooling efficiency. Accurate numerical simulations of this problem can help in identifying beneficial approaches to film-cooling design.

There have been numerous attempts to study film-cooling problem both experimentally and computationally. Among important observations of the researchers was strong dependence of the film-cooling flow on the geometry of the film-hole as well as the supply plenum. Simon et al.[1] studied the effect of the film hole length-to diameter ratio. Leylek et al.[2,3] investigated the effect of shaping of film holes. Peterson and Plesniak[4] showed the influence of the direction of the flow in the supply channel. The conclusion follows is that in order to predict the film-cooling flow with reasonable accuracy, one has to incorporate an exact geometry of the film-holes and the supply plenum in the simulations, and not substitute the cooling gas injection with some artificial boundary conditions.

It is possible to list several computational studies of film-cooling flows, where the exact geometry of the film-holes and the plenum was incorporated.[2,3,5] However, all these studies used the time-averaged (so called Reynolds-averaged) Navier-Stokes equations (RANS method). RANS simulations capture only the averaged flow variables and thus use relatively coarse mesh. It is a practical and commonly used method for simulating flows over complex geometries. However, due to the limited capability of RANS turbulence models, it does not provide an accurate prediction of flows with complex turbulent structures, as film-cooling flows. Large Eddy Simulation (LES) can resolve time-dependent turbulence structures directly and only requires a model for the subgrid-scale terms, which are more universal and easier to model. Numerical simulations of film-cooling flows using LES have also been attempted recently.[6,7] These studies even incorporated the film hole into the simulations. But, typically, unrealistically long delivery tubes were used and inflow parabolic profile was supplied at the beginning of the delivery tube, instead of modeling the supply plenum. As it

---

[*] Research Assistant, Department of Aeronautics and Astronautics, AIAA Member

[†] Professor, Department of Aeronautics and Astronautics and Department of Mechanical Engineering, AIAA Member

was shown by some researchers,[8,9] the connection between the plenum and the film-hole causes the flow to separate from the downstream wall of the film-hole and create a blockage effect, which pushes majority of the film-hole flow to exit into the crossflow from the upstream portion of the hole. This effect is especially pronounced when the hole is inclined. To capture these effects it is necessary to capture the full geometry.

Large Eddy Simulations of a film-cooling flow above the flat surface are presented in this paper. The simulations model the exact geometry of film-cooling experiments of Pietrzyk et al.[10] It includes large sink-type delivery plenum, periodic array of 11 short film-cooling holes with length-to diameter ratio of $L/d \sim 3.5$ and the crossflow section. Results of the simulations are analyzed and compared with the experimental data of Pietrzyk et al.[10]

II. Numerical method

Numerical method specially developed for this problem consists of coupled simulations using multiple computational codes. A fully compressible LES code is used in the area above the flat plate, while a low Mach number LES code is employed in the plenum and film holes. The motivation for using different codes comes from the essential difference of the nature of the flow in these different regions. The flat surface, which is being cooled, models the turbine blade surface, and compressibility effects are important for the flow above the turbine blade. In the plenum, on the other hand, compressibility effects are not only unimportant, but the actual Mach number is so low, that use of the compressible code in that region would significantly slow down the computations. Low Mach number code would therefore be a logical choice for the plenum/film-hole region. The two computational codes are described below.

A. Compressible code

Compressible code which is used in the region above the flat plate was developed by Z.Xiong.[11] Compressible Navier-Stokes equations in primitive variables are solved numerically using implicit time integration with an approximately-factorized difference scheme. The spatial discretization is achieved by mapping the body-fitted mesh coordinates from physical space (x, y, z) to the uniform computational space (ξ, η, ζ). Fourth-order accurate central-difference scheme is used for first - and second- derivatives in the computational space. Details of the numerical implementation of the compressible code can be found in Ref. 12.

B. Low Mach number code

Low Mach number code which is used in the plenum and film holes is due to C. Pierce.[13] The set of equations solved numerically is the low Mach number approximation of the Navier-Stokes equations written in conservative form in cylindrical coordinates. Velocity components are staggered with respect to density and other scalars in both space and time.[14] Second order central difference scheme is used for the integration of momentum equations, while QUICK scheme[15] is employed for scalar advection to avoid the formation of spatial oscillations. Second-order Crank-Nickolson scheme with sub-iterations is used for time advancement. Advection and diffusion terms in radial and azimuthal directions are treated implicitly. Poisson equation for pressure is solved with the multigrid method. For more details, the reader is referred to Ref. 13.

Both codes are written in LES formulation with dynamic Smagorinsky eddy-viscosity model[16] used for the treatment of subgrid-scale terms.

C. Combining the codes

The major challenge in combining compressible and low Mach number codes together is to specify an accurate and stable way of supplying the variables across the interfaces. In the present method, we use overlapping grids, where computational domain of one code has an area of overlap with the domain of another code. A sample computational domain, which includes the region above the leading edge of a turbine blade, and a film hole with a plenum, is shown in Fig. 1. Compressible code domain corresponds to the region exterior to the turbine blade and shown as striped in Fig. 1. Low Mach number code domain corresponds to a plenum and film hole in Fig. 1.

Only one boundary of the compressible code domain intersects the low Mach number code domain. This boundary is part of the turbine blade surface, and the intersection occurs at the place, where cooling gas is injected. Variables from the low Mach number code should be supplied to the compressible code at this location, which is schematically shown by the arrow 1 in Fig. 1. Boundaries of the low Mach number code domain which intersect the compressible code domain are shown in bold lines in Fig. 1. These are ”free” boundaries of the low Mach number code domain, since they are not part of film hole walls. Variables from the compressible code should be supplied to the low Mach number code at these boundaries, which is schematically shown by arrows 2 in Fig. 1.

1. Variables supplied from the low Mach number code to the compressible code

Variables, which are solved for in the compressible code, are $\{\rho, u, v, w, T\}$. All these variables should be specified at the location of cooling gas injection. Various ways of specifying these variables have been tested (the details of the test cases are described in[17]). However, the best performance was achieved by interpolating all of the variables $\{\rho, u, v, w, T\}$ from the low Mach number code.

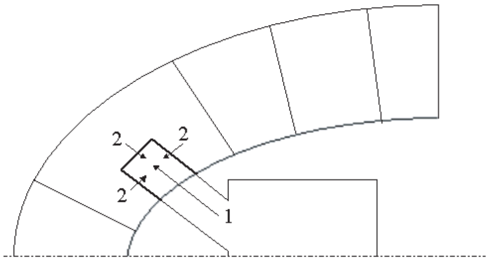

Figure 1. Sample computational domain for calculation of film-cooling geometry.

2. Variables supplied from the compressible code to the low Mach number code

In low Mach number code boundary conditions are required for the following variables. Momentum equations need values of three components of velocity $\{u, v, w\}$ at the boundaries. Scalar transport equation requires specification of a scalar (temperature) at the boundary. Density is obtained from temperature through the equation of state, therefore, no boundary conditions for density is required. $\{u, v, w, T\}$ are interpolated from compressible code at the ”free” boundaries of low Mach number code domain (boundary surfaces of low Mach number code domain intersecting compressible code domain). The same procedure is applied regardless of whether the ”free” boundary corresponds to an inflow or outflow.

In addition, we need boundary conditions for pressure for solving the Poisson equation. In the low Mach number approximation only the second order pressure $P^{(2)}(\vec{x}, t)$ enters the equations of motion (see, for example, Ref. 18). It is decoupled from density and temperature fluctuations and determined by the constraint on the divergence of velocity, much like the pressure in incompressible equations. Zeroth-order pressure $P^{(0)}(t)$ plays the role of the global thermodynamic pressure and enters the equation of state. Pressure field obtained in compressible equations is $P^{compr}(\vec{x}, t) = P^{(0)}(t) + P^{(2)}(\vec{x}, t)$. Taking gradient of P we have $\nabla P(\vec{x}, t) = \nabla P^{(2)}(\vec{x}, t)$.

In the present method, we solve the Poisson equation with Neumann boundary conditions for $P^{(2)}$. We specify the value of derivative $\frac{\partial P^{(2)}}{\partial \vec{n}}$ in the direction normal to the boundary surface. We interpolate $\frac{\partial P^{(2)}}{\partial \vec{n}} = \frac{\partial P^{compr}}{\partial \vec{n}}$ from the gradients of the compressible pressure field at the ”free” boundaries of low Mach number code domain intersecting the compressible code domain. Zeroth-order pressure $P^{(0)}$ is then added to the calculated field of $P^{(2)}$ in order to set the right value of the total static pressure. We find the value of $P^{(0)}$ by matching $P^{compr} = P^{(0)} + P^{(2)}$ at one specific location in the region of overlap.

Other choices for specifying boundary conditions at the ”free” boundaries of the low Mach number code domain are possible, for example, Dirichlet boundary conditions for the Poisson equation, normal derivatives for velocities instead of velocities itself. However, the method described above proved to work the best.

We use bilinear interpolation to interpolate values both from compressible to low Mach number code and from low Mach number to compressible code. Since the low Mach number code has a second-order accurate space discretization, increasing the order of interpolation beyond the second order does not lead to any further advantage.

The current method has been thoroughly tested on both steady and unsteady problems and shows good performance, which is documented in.[17]

III. Geometrical set-up of the problem

The geometry of the problem corresponds to the film-cooling experiments of Pietrzyk et al.[10] All geometrical scales in the problem are non-dimensionalized by the diameter of the film-hole d. Large cylindrical plenum with the height $20\,d$ and radius $10.526\,d$ feeds 11 cylindrical holes with length-to diameter ratio $L/d \sim 3.5$. Film-cooling holes are spaced uniformly in spanwise direction with the pitch $3\,d$. Film-holes are inclined at 35 degrees with respect to the flat surface.

Since the experiments[10] corresponds to a low speed flow we use a small value of Mach number $M = 0.15$ for the compressible code. However, Mach numbers are greater in the real gas turbine environment, so the use of compressible code in this region is completely justified.

The characteristics of the crossflow boundary layer in the absence of the cooling gas injection at $x/d = -2$ are summarized in Table 1. Here $\delta_{i,fc}$, $\delta^*_{i,fc}$ and $\theta_{i,fc}$ denote 99%, displacement and momentum boundary layer thicknesses at the inflow boundary of the film-cooling domain, respectively. $Re_{\theta_{i,fc}} = \frac{U_{fs}\theta_{i,fc}}{\nu}$ is the Reynolds number based on the free-stream velocity and $\theta_{i,fc}$. These characteristics correspond to a turbulent boundary layer. Since crossflow boundary layer is turbulent in both experiments,[10, 19] the use of a separate Large Eddy Simulation of turbulent boundary layer is required to generate the correct initial and boundary conditions.

$\delta_{i,fc}/d$	$\delta^*_{i,fc}/d$	$\theta_{i,fc}/d$	$Re_{\theta i,fc}$
0.52	0.089	0.059	946

Table 1. Crossflow boundary layer characteristics.

IV. Large Eddy Simulation of turbulent boundary layer

We use the rescaling and recycling technique of Lund et al.[20] to numerically compute the turbulent boundary layer. The idea of the recycling method bears its origin in the self-similarity of the boundary layer phenomenon. One needs to specify the target momentum thickness in the inflow and compute the flow up to some downstream location, called the reference- station. Then the mean streamwise velocity in the inner and outer layers at the inflow can be obtained from its value at the reference station from the following relationships

$$U_i^{inner} = \alpha U_r(y_i^+) \tag{1}$$

$$U_i^{outer} = \alpha U_r(\eta_i) + (1-\alpha)U_{fs}. \tag{2}$$

Here subscript i denotes the inflow, r - reference (or recycle) station and fs - free-stream conditions, $\alpha = u_{\tau i}/u_{\tau r} = (\theta_r/\theta_i)^{1/8}$, $u_\tau = \sqrt{\nu(\partial u/\partial y)_{wall}}$ is the friction velocity, $y^+ = (u_\tau y)/\nu$ is the wall coordinate and $\eta = y/\delta$ is the outer coordinate. Overall profile can be computed from the inner and outer values using appropriate weighting functions.

Some modifications to the method of Lund et al.[20] are required, since it was used in the incompressible setting, as opposed to current compressible simulations. Several techniques were proposed in order to extend this method to account for the flow compressibility.[21, 22] We use the modification of the method of Xu et al.,[21] slightly relaxed. Strictly speaking, mean streamwise velocity and temperature are coupled in the rescaling technique of Xu et al.[21] However, since Mach number in our simulations is quite small, we ignore this coupling and compute the streamwise velocity from Eqs. 1, 2. We then find the temperature T from the Walz's equation

$$\frac{T}{T_{fs}} = \frac{T_{wall}}{T_{fs}} + \frac{T_{rec} - T_{wall}}{T_{fs}}\frac{U}{U_{fs}} - r\frac{\gamma-1}{2}M_{fs}^2\left(\frac{U}{U_{fs}}\right)^2, \tag{3}$$

where T_{rec} is the recovery temperature $T_{rec} = T_{fs}(1 + r(\gamma-1)/2)M_{fs}^2$, γ is the ratio of specific heats and $r = \sqrt{Pr}$ is the recovery factor. Mean density can be found from the equation of state and mean temperature. Mean vertical velocity and velocity fluctuations can be rescaled as

$$(V)_i = \alpha \sqrt{\frac{\rho_{walli}}{\rho_{wallr}}} \sqrt{\frac{\rho_r}{\rho_i}} (V)_r$$

$$(u'_j)_i = \alpha \sqrt{\frac{\rho_{walli}}{\rho_{wallr}}} \sqrt{\frac{\rho_r}{\rho_i}} (u'_j)_r$$

Index $j = 1, 2, 3$ corresponds to u', v', w'. These relationships should be applied for $y_r^+ = y_i^+$ for inner layer and $\eta_r = \eta_i$ for outer layer. Temperature and density fluctuations deserve a special attention, and a scaling law for these quantities can be found in Ref.21.

Turbulent boundary layer calculations in References[20–22] were initialized by setting all the variables to the sum of their mean values and random fluctuations with the amplitude of 10% of the mean values. However, it was found in our simulations that failure to specify the correct energy spectra of the initial turbulence field leads to the fast decay of the disturbances. Similar observations were made by Ferrante et al.[23] Therefore, special numerical procedure, which reconstructs realistic turbulence fluctuations from the specified spectra[12, 24] is employed. These fluctuations are than rescaled according to the boundary layer intensity profiles (which can be taken from experiments) and added to the mean quantities. This procedure allows to avoid the decay of initial disturbances and ensures shorter computational time for the realistic turbulence field to develop.

The computational domain for LES of turbulent boundary layer has dimensions $7.5d \times 2d \times 3d$ with the inflow boundary located at $x/d = -4$. Present simulations are controlled by specifying target inflow boundary layer thickness $\delta_i/d = 0.48$ in order to achieve the desired $\delta_{i,fc}/d = 0.52$ for the film-cooling LES at $x/d \sim -2$. Recycling station is located at $x/d \sim 1.5$. Rescaled with δ_i, the computational domain for LES of turbulent boundary layer has dimensions $15\,\delta_i \times 4\,\delta_i \times \pi/2\,\delta_i$. The grid $128 \times 128 \times 32$ is used in the simulations, resulting in the resolution $\Delta x^+ \approx 38, \Delta y^+_{wall} \approx 0.6$ and $\Delta z^+ \approx 16$. The grid is uniform in streamwise and spanwise directions, while hyperbolic-tangent stretching function is used in the wall-normal direction.

Numerical method employed in compressible LES code uses fourth-order central difference discretization for spatial terms. Because of the symmetric stencil such a scheme by itself is non-dissipative. The lack of any dissipation in large eddy simulations of turbulence can result in numerical instability due to the generation of unresolved high wave number components by nonlinear flow interactions. In order to damp these unresolved components, a fourth-order artificial dissipation is introduced by adding the following term to the right-hand side of Navier-Stokes equations

$$\vec{D} = -\epsilon_d \sigma_d(\xi, \eta, \zeta)(\Delta\xi^4 \frac{\partial^4 \vec{U}}{\partial \xi^4} + \Delta\eta^4 \frac{\partial^4 \vec{U}}{\partial \eta^4} + \Delta\zeta^4 \frac{\partial^4 \vec{U}}{\partial \zeta^4}), \tag{4}$$

where $\vec{U} = (\rho, u, v, w, T)^T$ is the vector of flow variables, ϵ_d is the amplitude of the added dissipation and the grid-dependent quantity $0 \leq \sigma_d(\xi, \eta, \zeta) \leq 1$ controls the range of the dissipation. If the value of the amplitude ϵ_d is chosen to be too large, artificial dissipation will result in damping resolved turbulence fluctuations in addition to unresolved high wave number components and severely deteriorate the solution. It was found by Xiong[12] that in order for the magnitude of the added dissipative terms to be much smaller than the value of the truncation error of a spatial discretization scheme, the coefficient ϵ_d should satisfy the condition $\epsilon_d h < 0.01$, where h is the maximum distance between two adjacent grid nodes. However, this condition applied to LES of turbulent boundary layer was not sufficiently strict and resulted in excessive damping of turbulent kinetic energy. Further reduction of the coefficient to $\epsilon_d h < 0.002$ was needed, giving the estimate $\epsilon_d < 0.034$ for the present grid. $\epsilon_d = 0.03$ was used in the simulations with the uniform distribution of dissipation $\sigma_d(\xi, \eta, \zeta) \equiv 1$, leading to the total value of the added dissipation $\epsilon_d \sigma_d = 0.03$ everywhere in the domain.

Snapshots of instantaneous spanwise velocity in $x - y$ and $y - z$ planes are shown in Fig. 2.

Turbulence intensity profiles u'^+, v'^+, w'^+ are plotted in Fig. 3(a) versus y/δ. Results of the current LES are compared with the DNS of turbulent boundary layer performed by P. R. Spalart[25] at $Re_\theta = 670$. The agreement is very good close to the wall. Intensities are slightly overpredicted in the outer part of the boundary layer with peak value of u'^+ higher than the one obtained by Spalart. Disagreement may be due to the difference in Reynolds numbers of Spalart simulations with $Re_\theta = 670$ and current calculations with $Re_\theta = 946$.

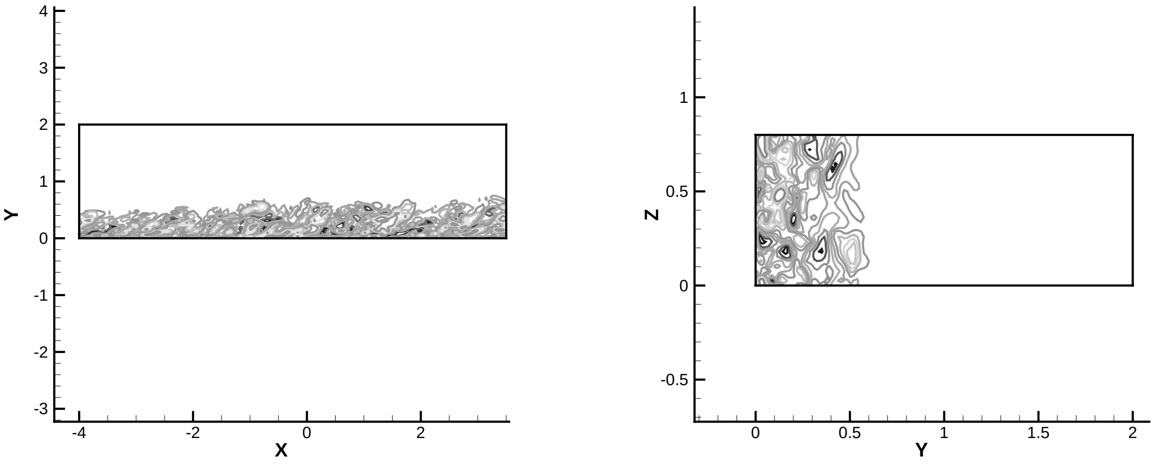

(a) $x - y$ plane

(b) $y - z$ plane

Figure 2. Instantaneous spanwise velocity for LES of boundary layer.

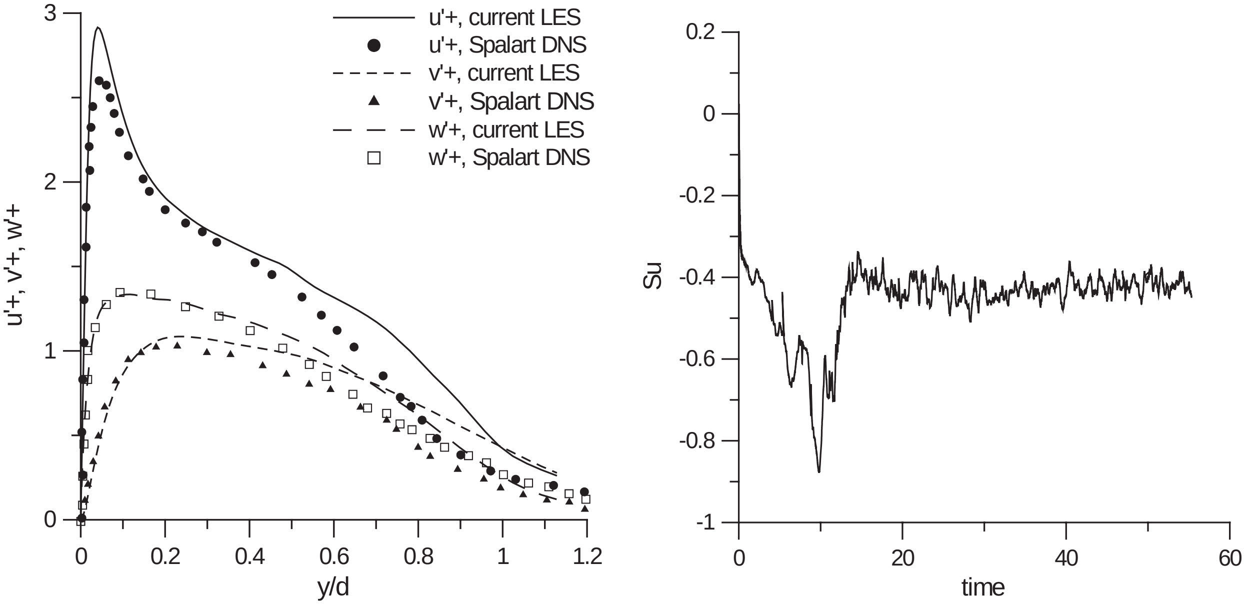

(a) Turbulence intensity profiles

(b) Time-development of the velocity-derivative skewness

Figure 3. Turbulent boundary layer characteristics.

We plot the value of velocity-derivatives skewness defined as

$$S_u = [\frac{1}{3}\sum_{i=1}^{3}\langle(\partial u_i'/\partial x_i)^3\rangle][\frac{1}{3}\sum_{i=1}^{3}\langle(\partial u_i'/\partial x_i)^2\rangle]^{-\frac{3}{2}}, \tag{5}$$

averaged over the whole length and width of the domain and a height of $0 \leq y \leq 0.7\delta_i$ versus non-dimensional time tU_{fs}/δ_i in Fig. 3(b). This skewness is related to the process of vortex stretching and nonlinear energy transfer from small to large wavenumbers. It was shown by Ferrante et al.[23] that unless a realistic turbulent kinetic energy spectrum is specified in the initial conditions, the calculations are not able to sustain the required magnitude of the cross correlation $\langle u'v' \rangle$ necessary for the production of turbulent kinetic energy and the value of S_u vanishes as time increases. Value of S_u stays equal to about -0.5 in their DNS of turbulent boundary layer at $Re_\theta = 1430$ with improved initial conditions. In the present calculations the velocity-derivative skewness maintains a value of about -0.4 after some initial transient, which shows that the proper energy transfer rate is sustained throughout the simulations.

V. Large Eddy Simulation of film-cooling flow

A. Computational domain and boundary conditions

Computational domain for the compressible code is the box with dimensions $7.5\,d \times 2\,d \times 3\,d$. The cooled surface is a flat plate spanning the range $x/d = (-2; 5.5)$, where the point $(x/d = 0, y/d = 0)$ is located on the wall at the leading edge of the jet. Because of the elliptical shape of the hole, the trailing edge is located at $x/d = 1.74$. The grid with $128 \times 128 \times 128$ nodes is used in the simulations. Hyperbolic-tangent stretching is utilized in wall-normal direction to cluster points in the wall boundary layer. Uniform grid is used in streamwise and spanwise directions due to the occurrence of high-intensity fluctuations at any location after the cooling gas injection. The plenum and the film hole use $256 \times 128 \times 64$ and $128 \times 64 \times 64$ grid points respectively. Only one hole is simulated here, however, periodic boundary conditions in spanwise direction make it similar to the periodic array of holes. Overlap regions exist between both plenum and a film hole and between a film hole and a compressible domain. Plenum is coupled to the film hole by the same coupling procedure as described in subsection C, but applied to two low Mach number codes. $x - z$ view of the computational domain used in the simulations is shown in Fig. 4.

Uniform velocity profile $U_{plenum} = 0.0029$ is specified at the entrance into the plenum. This flow rate results at the mean velocity $U_j = 0.737$ at the pipe exit giving the value for the velocity ratio $VR = \frac{U_j}{U_{fs}} = 0.737$, where U_{fs} is the crossflow free-stream velocity. Following heat transfer experiments of Bons et al.[19] we use density ratio $DR = \frac{\rho_j U_j}{\rho_{fs} U_{fs}} = 0.95$. This leads to blowing ratio $B = \frac{\rho_j U_j}{\rho_{fs} U_{fs}} = 0.7$ and momentum ratio $I = \frac{\rho_j U_j^2}{\rho_{fs} U_{fs}^2} = 0.52$.

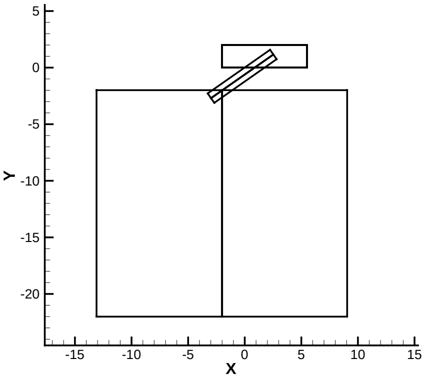

Figure 4. $x - z$ view of of the computational domain for LES of film-cooling.

The rest of the boundaries of the plenum and the pipe correspond to either walls with no-slip and adiabatic boundary conditions applied or boundaries of the overlapping region, where interface boundary conditions are set according to C. For the compressible code domain we use no-slip adiabatic boundary conditions for the wall, interface conditions C in the region of jet injection, uniform free-stream at the top and parabolized Navier-Stokes equations at the outflow. To get inflow turbulent boundary layer quantities we use auxiliary code performing LES of turbulent boundary layer simultaneously with the main simulations. We first obtain developed turbulent boundary layer on the narrower domain with a width $0.8\,d$ as described in section IV. Then we stack together four different realizations of this simulation and rescale the width of the resulted domain to obtain the desired value of $3\,d$. After some initial transient the irregularities in the places of the domains attachment smooth out, and the correct spanwise development of turbulent boundary layer is recovered. To demonstrate it, instantaneous spanwise velocity for the domain of width $3d$ is plotted at Fig. 5 in the $y-z$ plane. The places where domains were connected are no longer distinguishable. Afterwards, variables taken at the point $x/d = 0$ of the turbulent boundary layer domain, corresponding to $\delta/d = 0.52$ are supplied at every time step through Riemann invariants at the inflow boundary of the film-cooling domain.

The same artificial dissipation scheme as in the LES of turbulent boundary layer (see Eq. 4) is used in film-cooling simulations for the compressible code. However, due to sharp gradients of flow variables at the place where the film-cooling jet enters the compressible domain, the value for the artificial dissipation $\epsilon_d \sigma_d = 0.03$ was not sufficient to sustain numerical stability. Some variation of the function $\sigma_d(\xi, \eta, \zeta)$ is required to adjust the total value of the added dissipation $\epsilon_d \sigma_d$, so it reaches the maximum at the place of the jet injection and gradually decreases to the required value of ~ 0.03 away from it. An ad-hoc function was used in the current simulations. However, a new method where the coefficient of artificial dissipation automatically adjusts locally depending on high-order derivatives of the strain-rate tensor without introducing any ad-hoc assumptions [26–28] is currently under development.

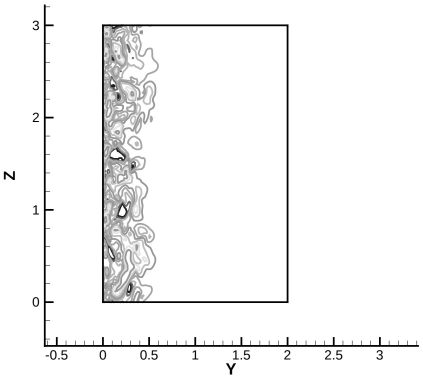

Figure 5. Instantaneous spanwise velocity for boundary layer LES at $y-z$ plane for the domain with the width $3d$.

B. Simulation results

1. *Instantaneous quantities*

To visualize the flow behavior pertinent to the plenum-jet-crossflow interaction, instantaneous streamlines are plotted at the $x-z$ centerplane in Fig. 6. Reverse flow is noticeable in the pipe region right after the exit from the plenum in Fig. 6(a). This reverse flow is created by the sharp turning of the flow exiting the plenum and encountering an inclined hole, which leads to the flow separation and formation of the low-momentum region near the windward wall of the film hole. This separation gives rise to the so-called blockage effect forcing the majority of the pipe flow exit from the leading edge part of the jet cross-section. This effect is related to the presence of plenum and shortness of the film hole and is more pronounced for shorter holes and higher blowing ratios. Another effect influences the jet exit velocity profile - the blockage of the crossflow by the incoming jet. This blockage results in the non-uniform pressure distribution at the jet exit plane with high pressure at the leading edge of the cross-section and low pressure at the trailing edge. High pressure at the leading edge forces the pipe flow to exit from the trailing edge. The two effects are counteracting each other and the resulting jet exit velocity profile mainly depends on the specification of the film-cooling configuration, such as blowing ratio and L/d. It was documented by Leylek and Zerkle[8] that for low L/d and blowing ratio about $B \sim 0.7$ the maximum of the jet exit velocity profile occurs close to the middle of the cross-section, but shifted a little bit upstream. The same is observed in the current simulations, where the majority of the jet flow exits neither from leading nor trailing edge, but from the narrow area close to the jet centerline. Further confirmation of this effect can be illustrated by looking at instantaneous streamlines at the orthogonal view within the film hole at the location shown in Fig. 6(a). These streamlines are illustrated in Fig. 7(a). The swirling flow is again noticeable with quite irregular pattern at the windward side of the jet. Instantaneous contours of vertical velocity at the elliptical jet exit cross-section (where inclined jet intersects the flat plate) are shown in Fig. 7(b). Largest values of vertical velocity occur a little bit upstream from the center part of the cross-section, in agreement with our earlier observations.

Streamlines at the cross-flow region after the film-cooling flow injection are shown in Fig. 6(b). Reverse flow zone right behind the trailing edge of the exiting jet is clearly pronounced. Although this effect was not clearly observed but only hypothesized in experiments,[10] RANS simulations of the same geometrical configuration by Walters and Leylek[2] with $B = 1$ and $DR = 2$ managed to resolve this reversed flow zone using a more accurate two-layer turbulence model. Moreover, detailed experimental and computational studies of jets in crossflow found this reverse flow to be a common feature of the jet and a crossflow interaction explained by the entrainment of the crossflow fluid moving around the jet into the wake of the jet by the low pressure zone created beneath it. It is perhaps more clearly illustrated in Fig.8, where two streamlines

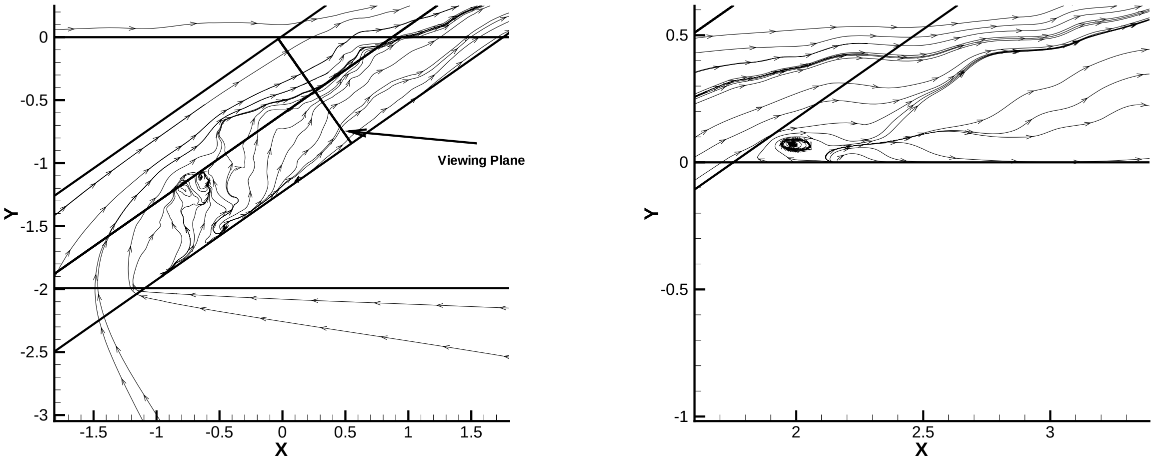

(a) In the pipe

(b) In the crossflow right after the jet injection

Figure 6. Instantaneous streamlines in $x - z$ centerplane.

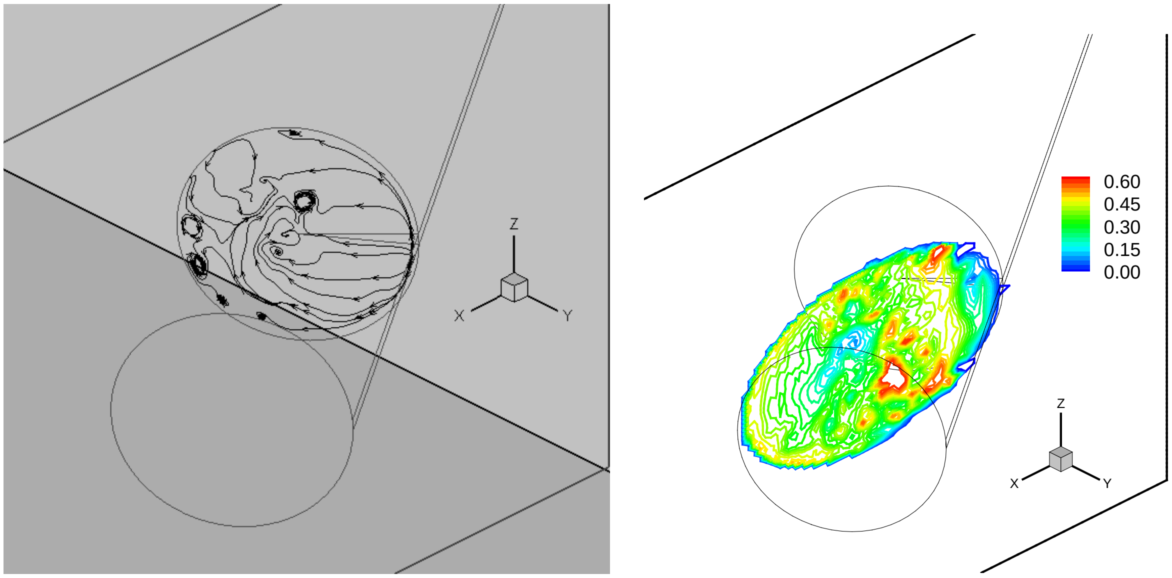

(a) Instantaneous streamlines at the cross-sectional plane within film hole

(b) Contours of instantaneous vertical velocity at the jet exit

Figure 7. Details of jet exit velocity profile.

originating from the crossflow boundary layer ($y/d \sim 0.07$) and just off the side of the jet ($(z - z_c)/d = \pm 0.6$) are shown in three dimensions (here $z_c/d = 1.5$ is the spanwise coordinate of the jet centerline). Vertical velocity contours at the bottom surface of the domain are also plotted here to mark the location of the jet exit. It is seen how the streamlines reverse back around the jet and are being lifted up into its wake. This effect is far less pronounced for inclined jets than in the case of normal jets, because the blockage of the crossflow by the jet responsible for this effect is much weaker when the jet is inclined. This reverse flow is responsible for bringing hot crossflow fluid underneath the jet and results in the decrease of film-cooling effectiveness right after the jet exit, observed in experiments.[29]

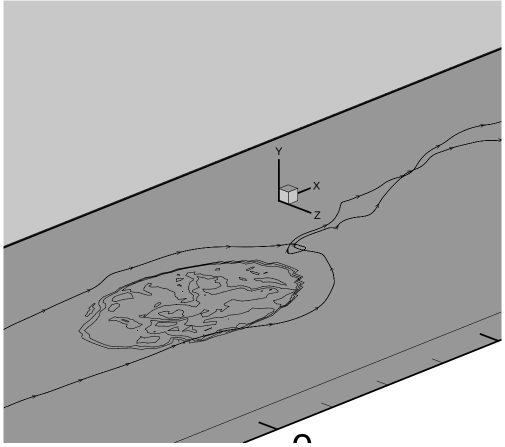

Figure 8. Three-dimensional streamlines showing the effect of lift up.

Film-cooling effectiveness is the measure of the performance of the given cooling configuration and is defined as $\eta = \frac{T_{aw} - T_{fs}}{T_j - T_{fs}}$. Here T_{aw} is the adiabatic wall temperature, T_{fs} is the free-stream temperature of the crossflow, T_j is the temperature of the coolant injectant. Instantaneous snap-shot of the normalized temperature $\frac{T - T_{fs}}{T_j - T_{fs}}$ in the center-plane is plotted in Fig. 9(a). The region of reduced effectiveness at the wall right behind the jet is caused by the entrainment of hot crossflow fluid underneath the jet and is clearly noticeable. The streamwise plot of centerline effectiveness η_c is shown in Fig. 9(b). The value of η_c drops significantly, reaching the value of 0.2, then slightly increasing back to about 0.6. This behavior is referred to as detachment-reattachment of the jet by Sinha et al.[29] It is also noted by the same authors that detachment-reattachment effect scales with momentum flux ratio. Momentum ratio $I = 0.52$ at the present simulations is indeed quite large for film-cooling applications and makes this effect pronounced for all density ratios. Comparing the present plot with time-averaged centerline effectiveness in Ref. 29 for $I = 0.5$ and $DR = 1.2$, which is the closest to the present simulations, we indeed find the similar drop-off to about 0.3 or so. The minimum value of η_c seems to decrease with DR and therefore is expected to be even smaller for $DR = 0.95$ consistent with our observations. However, the centerline effectiveness recovers to only about 0.35 in Ref. 29, not to 0.6. This might be explained by time-averaging which will smooth out the instantaneous peak values.

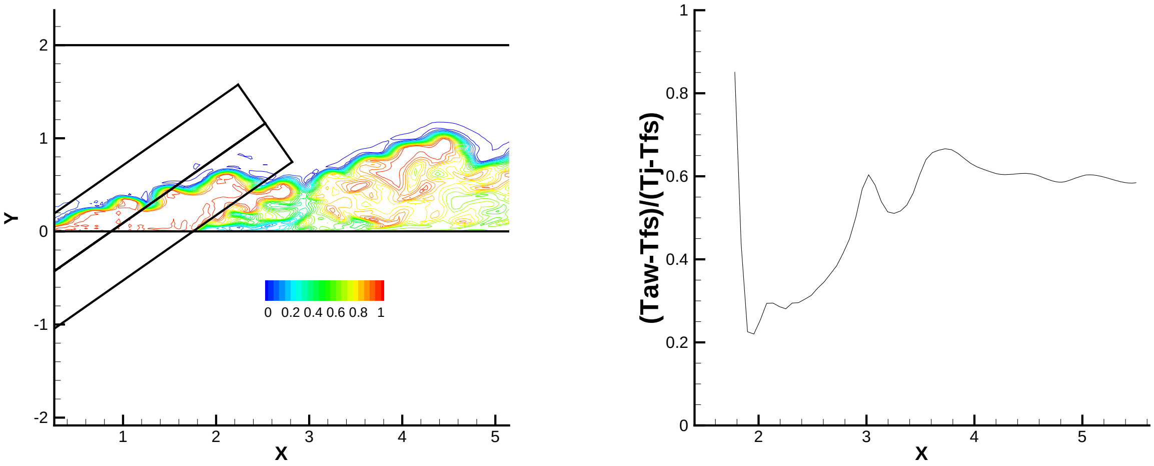

(a) Snapshot of $\frac{T - T_{fs}}{T_j - T_{fs}}$ at $x - y$ centerplane

(b) Plot of instantaneous centerline effectiveness versus streamwise distance

Figure 9. Instantaneous film-cooling effectiveness.

To look at vorticity dynamics we plot instantaneous normalized transverse vorticity $\omega_z \, d/U_{fs}$ in $x - y$

centerplane in Fig.10 in the crossflow region. Two shear layers are noticeable - one with positive vorticity at the leading edge of the jet, and another with negative - at the trailing edge. As opposed to the normal jet injection (see Ref. 17), they do not quickly merge together in the single shear layer. Instead, they follow their own pathes, merging much later at about $x/d \sim 4$, which is consistent with experiments.[10] The high levels of vorticity in the upper shear layer disappear much more rapidly than in the lower one, indicating fast mixing between the top part of the jet and the crossflow. High vorticity spots also exist in the middle of the jet exit, corresponding to the vortices shed during the flow separation in the pipe and exiting mainly form the center of the jet, as previously noticed at Fig. 6(a). The two shear layers and high vorticity fluctuations in the middle of the pipe correspond to the regions of high turbulence production identified in experiments .[10] There is also region of positive vorticity which occurs in the wake of the jet beneath the lower shear layer. This positive vorticity is brought from the upper shear layer by the crossflow fluid which goes around the jet and being lifted up into the wake by the low pressure region. This is consistent with the similar observations found in normal jets. The layer of negative vorticity beneath it correspond to the boundary layer vorticity.

To look at the spanwise development of the jet we plot instantaneous vertical vorticity contours $\omega_y\, d/U_{fs}$ in Fig.11 at the three horizontal cross-sections: $y/d \sim 0.015$, $y/d \sim 0.22$ and $y/d \sim 0.45$. The second and third cross-sections are also shown in Fig.10. First cross-section is located very close to the wall. High values of vertical vorticity in the center of the jet exit is noticeable corresponding to the turbulent flow coming out of the pipe. Shear layers at both sides of the jet are created due to the mismatch of the streamwise velocity of the jet and a crossflow. However, spatially stationary and steady counter-rotating spanwise vortical structures such as DSSN vortices discovered close to the wall in normal jets[4, 17, 30] seem to be absent for the inclined jet and wall vorticity pattern is more irregular. Higher irregularity in vertical vorticity pattern close to the wall might also be attributed to the presence of turbulent boundary layer with high vorticity fluctuations already existing before the jet injection. Cross-section $y/d \sim 0.22$ comes through the wake of the jet. Mostly, vorticity of the negative sign prevails for $(z - z_c)/d < 0$ and of the positive sign for $(z - z_c)/d > 0$. Cross-section $y/d \sim 0.45$ penetrates the shear layer vortices above the wake. Vortices of the alternating sign are being shed on either side of the jet centerline. This is consistent with the observation of two different vortical structures pertinent to normal jets:[17] wake and shear-layer vortices with different origin and characteristics. However, vertical separation between the wake and the trailing edge shear layer is smaller in the case of inclined jet and a difference in both streamwise and vertical momentum between jet and crossflow is not as severe. Therefore, all these coherent vortical structures are far less pronounced and hard to distinguish.

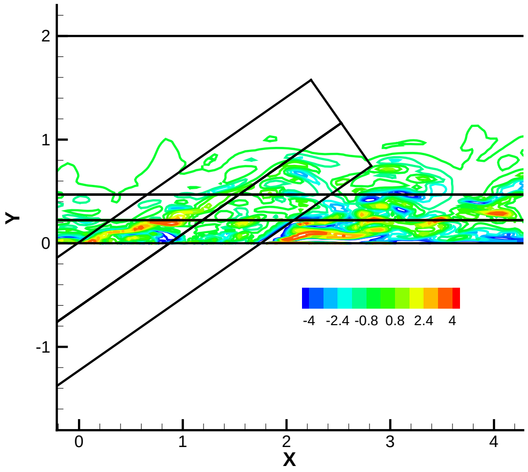

Figure 10. Instantaneous transverse vorticity, $\omega_z\, d/U_{fs}$, in $x - y$ centerplane.

2. Time-averaged quantities and comparison with experiments

Profiles of the normalized mean velocity vectors for the near-hole region of the jet exit at the centerplane are plotted in Fig. 12. Experimental profiles[10] for both $B = 0.5$ and $B = 1$ are shown in Fig. 13. Blowing ratio for the simulations $B = 0.7$ lies between the two experimental values. The edges of the jet are marked by the two streamlines originating from the leading edge and the trailing edge of the jet exit, respectively. Mean flow just above the jet exit seems relatively uniform with velocity vectors parallel to the walls of the film hole, resembling $B = 0.5$ experimental case. Downstream of the hole, the "wake region" is formed by the blockage of the jet. Mean velocity vectors pointed to the wall right after the jet exit indicate the formation of the reverse flow region documented previously (see Figs. 6(b) and 8 showing the instantaneous streamlines). Similar effect is visible on the experimental profiles for $B = 1$. Such an effect likely exists for $B = 0.5$ as well, but is not captured on the experimental images due to its relative weakness. The formation

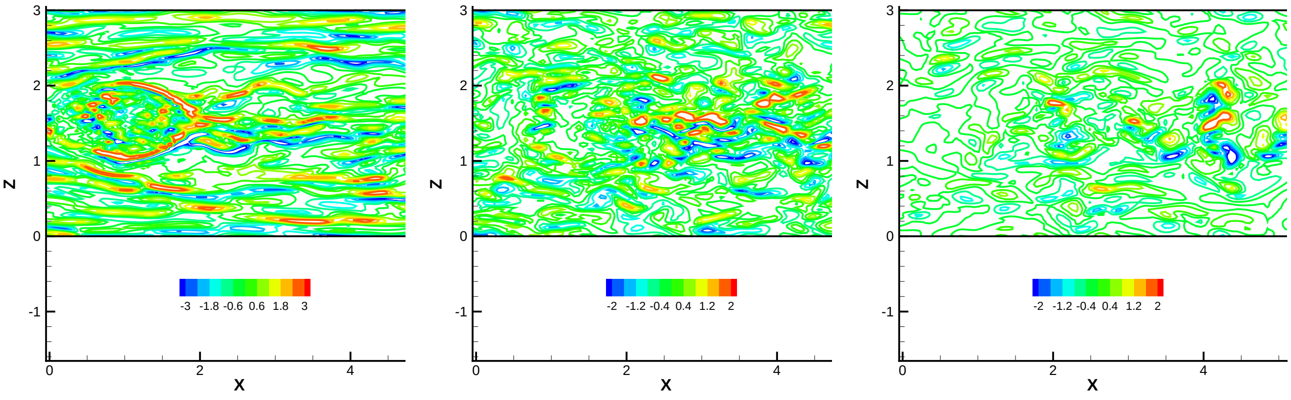

(a) $y/d \sim 0.015$ (b) $y/d \sim 0.22$ (c) $y/d \sim 0.45$

Figure 11. Instantaneous vertical vorticity, $\omega_y\, d/U_{fs}$.

of the strong shear layer between the low speed fluid in the wake and the lower edge of the jet is clear in the simulations and both experiments. The mean streamline originating from the trailing edge exactly follows this shear layer. Mean velocity profiles $U(y)$ have a point of local minimum at the location where this shear layer occurs. The top shear layer between the crossflow and the upper part of the jet is weaker and not as well pronounced in both simulations and experiments, except for the region right after the jet injection. This relative weakness of the top shear layer is also noticeable in the instantaneous transverse vorticity field, which decays fast after the jet injection (see Fig. 10). A lateral influx of the high-speed crossflow fluid below the jet into the wake region is indicated in the simulations and both experiments by a negative velocity gradient near the wall evident for $x/d > 3$.

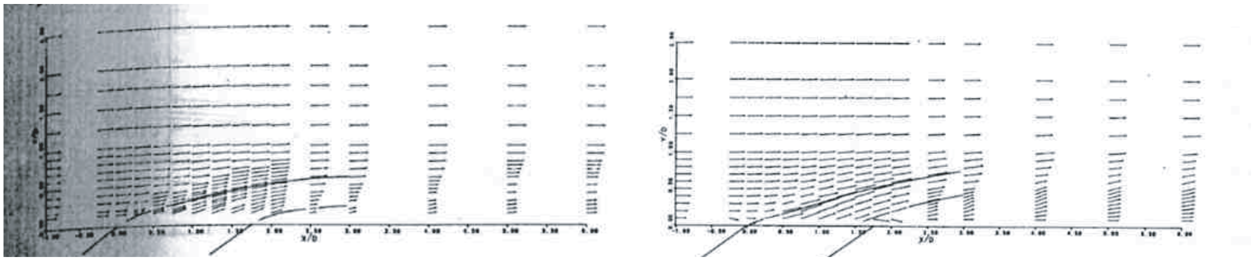

(a) $B = 0.5$ (b) $B = 1$

Figure 13. Normalized mean velocity vectors at the centerplane. Experimental profiles.

Turbulence statistics presented in this paper was collected over non-dimensional time $tU_{fs}/d \sim 2$. Although this gives an opportunity to look at preliminary results, definitive comparison with the experimental data can only be done when fully converged statistics become available.

Turbulence quantities in experiments^{10} were reconstructed by measuring the two components of the fluctuating velocity, u'_{rms} and v'_{rms}. They are presented in terms of a turbulence level (TL) defined as $TL = (u'^2_{rms} + v'^2_{rms})^{1/2}/U_{fs}$. The values of TL at the centerplane obtained in the simulations are plotted in Fig. 14. The same values corresponding to experiments^{10} with $B = 0.5$ and $B = 1$ are plotted in Fig. 15. Three major zones of turbulence production are identified in both simulations and experiments. First one is at the upstream edge of the jet as it exits the film-hole, with turbulence levels about 18%. The turbulence in this region is being produced by the shear layer between the top part of the jet and a

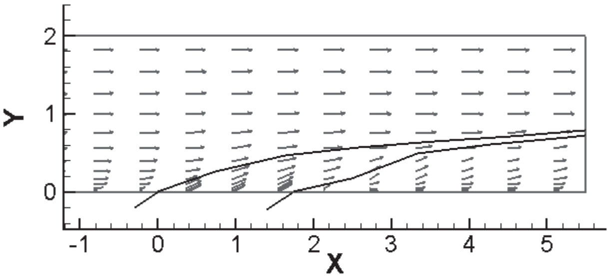

Figure 12. Normalized mean velocity vectors at the centerplane. Simulation profiles, $B = 0.7$.

crossflow. As it was noticed before, this shear layer diffuses quickly, resulting in a short extent of this region of high turbulence. The second zone is located at the center of the jet exit plane with 18% turbulence level for $0.5 \leq x/d \leq 0.7$. This turbulence is originated inside the film-hole due to the flow separation from the downstream wall and the jetting effect. Similar turbulence levels were found inside the film-hole in RANS simulations of Leylek and Zerkle.[8] The highest turbulence levels, reaching as much as 32%, are observed in the shear layer between the lower part of the jet and the wake. These high values are contained within a very small region, not distinguishable in Fig. 14, due to the lower plotted maximum contour levels. The contour levels of about 24%, however, spread the distance $2 \leq x/d \leq 2.5$. Region with $TL \sim 18\%$ lasts till $x/d \leq 3.2$. Another local region of high turbulence with 22% level can be noticed in the wake of the jet below the shear layer at $x/d \sim 3$, $y/d \sim 0.15$. This region corresponds to the region of high positive transverse vorticity (see Fig. 10), which identifies the location of the beginning of crossflow fluid entrainment into the wake. This zone has not been identified in the experiments. The qualitative pattern of turbulence level contours is more similar to $B = 0.5$ experiments, than to $B = 1$. Vertical extent of the region with $TL \geq 4\%$ is about $y/d \sim 1$ at $x/d = 4$ in the simulations. It is about $y/d \sim 0.9$ for $B = 0.5$ experiments and $y/d \sim 1.3$ for $B = 1$. However, largest values of TL in all three regions are higher in the simulations (which used $B = 0.7$) than experiments with $B = 0.5$, but lower than for $B = 1$ (except for the region with the highest level of 32%, which was probably not resolved in experiments due to its high localization). Some qualitative differences also exist, such as the shift of both first and second zones of turbulence production a little bit upstream and much faster decay of the turbulence levels in the bottom shear layer. These disagreements might be connected to the insufficient time for collecting the turbulence statistics in the simulations.

Contours of the $u'v'/U_{fs}^2$ shear stress near the jet exit are shown in Fig. 16 for the simulations and Fig. 17 for $B = 0.5$ experiments. The highest negative shear stress (~ -0.007) is observed at the interface between the jet fluid and the low velocity wake beneath the jet. The value and the location of this negative shear stress agree very well with the experiment. However, positive shear stress of approximately equal value ($\sim +0.007$) is also visible in the calculations inside the wake of the jet. It is probably connected to the presence of higher-momentum crossflow fluid in the wake and is in perfect agreement with the mean velocity profile in the wake, which shows negative velocity gradient near the wall (see Fig. 12). This positive shear stress is not highlighted in the experiments. Another region of high local shear stress is inside the film hole, which is consistent with the high level of turbulence found in this region and is also observed in experiments. Both positive and negative levels of $u'v'/U_{fs}^2$ exist inside the film hole, with negative values (up to -0.007) being larger than the positive ones ($\sim +0.003$), consistent with the experiments. We would like to stress out again the limited length of computational data available for the turbulence statistics so far. The longer averaging time will smear out some evident spatial fluctuations in both TKE and shear stress level.

VI. Conclusions

The experimental set-up of Pietrzyk et al.[10] is modeled numerically, using Large Eddy Simulation technique. To the author's knowledge, it is the first LES of film-cooling type flows, which includes the exact geometry of both the cooling hole and the plenum. Additional LES of turbulent boundary layer is performed in order to obtain initial and inflow boundary conditions for the main simulations. Velocity field inside the film-hole as well as at the crossflow region is analyzed. Reverse flow zone is observed at the pipe strongly influencing the jet exit velocity profile. Vorticity dynamics of inclined jet in a crossflow shows some similarity with that of a normal jet, however most of the coherent vortical structures are less pronounced. Entrainment of the cross-flow fluid beneath the jet exists at the present simulation regime causing the decrease in film-cooling effectiveness right behind the jet. Time-averaged velocity field as well as turbulence statistics is compared to the experimental values. The agreement between the mean velocity contours in the centerplane is very good. Similar pattern and magnitude of in-plane turbulence kinetic energy and shear stress is observed both in simulations and experiments with some minor differences. The length of flow time over which the turbulence statistics have been collected thus far is $t\,U_{fs}/d \sim 2$. Longer averaging times are needed for convergence of the statistics, especially the Reynolds stresses. This is planned for the near future.

VII. Acknowledgements

This work is supported by the Advanced Simulation and Computing (ASC) program of the Department of Energy. The compressible code was developed with AFOSR support under grant No. F94620-01-1-0138.

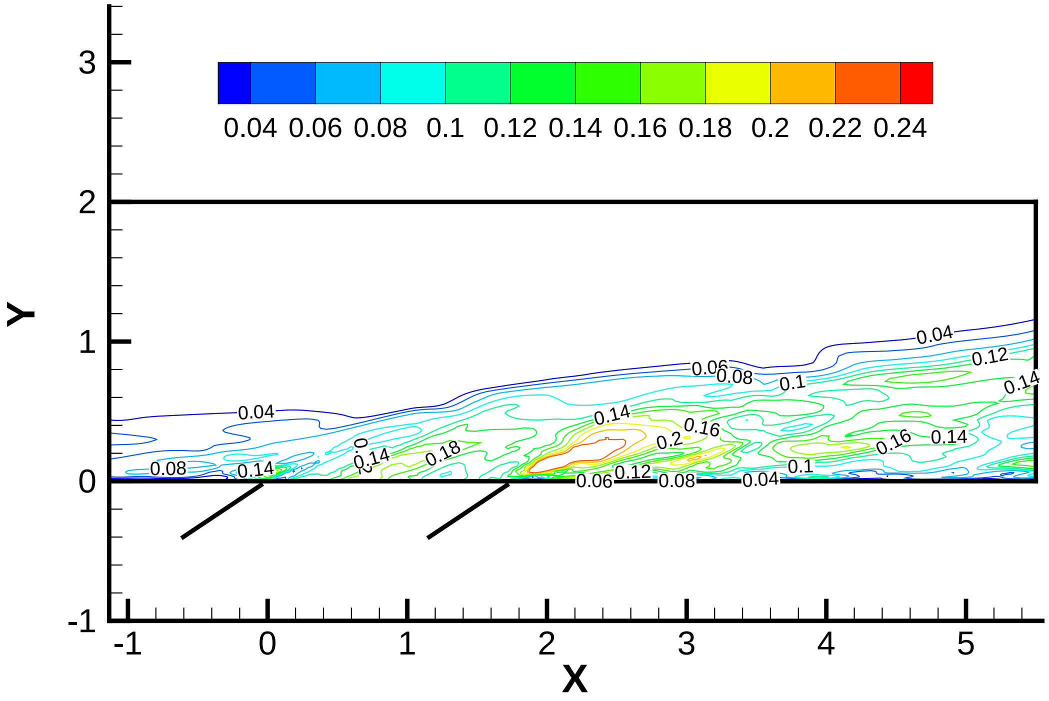

Figure 14. Turbulence level, $(u'^2_{rms} + v'^2_{rms})^{1/2}/U_{fs}$, contours at the centerplane. Simulation results.

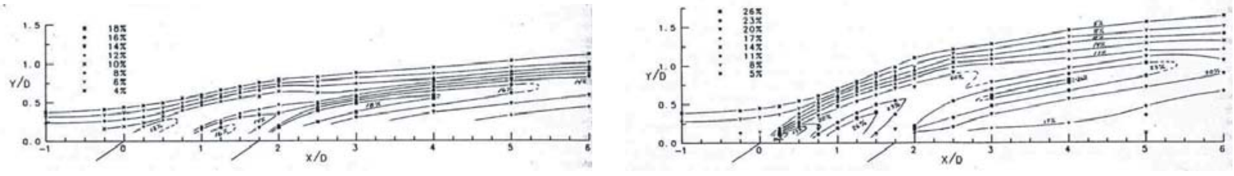

(a) $B = 0.5$

(b) $B = 1$

Figure 15. Turbulence level, $(u'^2_{rms} + v'^2_{rms})^{1/2}/U_{fs}$, contours at the centerplane. Experimental results.

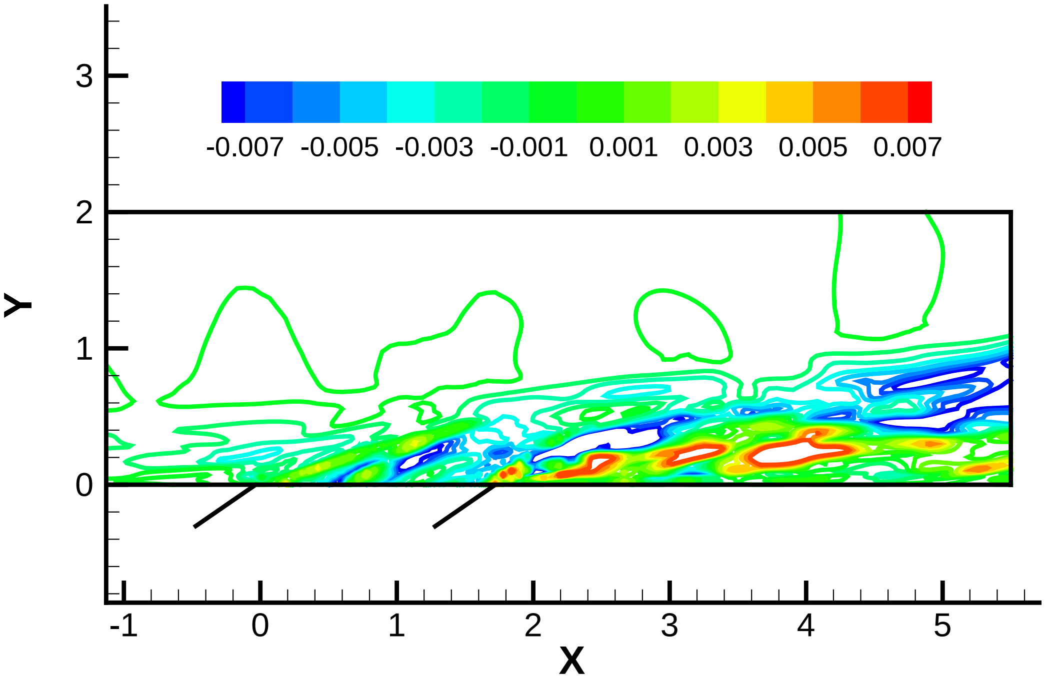

Figure 16. Shear stress, $u'v'/U_{fs}^2$, contours at the centerplane. Simulation results.

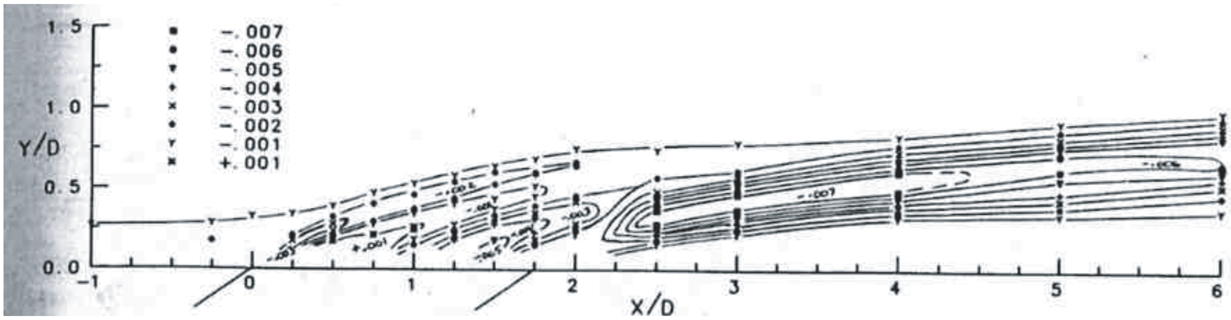

Figure 17. Shear stress, $u'v'/U_{fs}^2$, contours at the centerplane. Experimental results. $B = 0.5$.

Computer time is provided by ARL and ERDC High-Performance Supercomputer Centers at the Department of Defense.

References

[1] Burd, S. W., Kaszeta, R. W., and Simon, T. W., "Measurements in Film Cooling Flows: Hole L/D and Turbulence Intensity Effects," *Transactions of the ASME. The Journal of Turbomachinery*, Vol. 120, Oct. 1998, pp. 791–798.

[2] Walters, D. K. and Leylek, J. H., "A Detailed Analysis of Film-Cooling Physics: Part I - Streamwise Injection With Cylindrical Holes," *Transactions of the ASME. The Journal of Turbomachinery*, Vol. 122, Jan. 2000, pp. 102–112.

[3] Hyams, D. G. and Leylek, J. H., "A Detailed Analysis of Film-Cooling Physics: Part III - Streamwise Injection With Shaped Holes," *Transactions of the ASME. The Journal of Turbomachinery*, Vol. 122, Jan. 2000, pp. 122–132.

[4] Peterson, S. D. and Plesniak, M. W., "Evolution of Jets Emanating from Short Holes into Crossflow," *Journal of Fluid Mechanics*, Vol. 503, 2004, pp. 57–91.

[5] Bohn, D., Becker, V., and Kusterer, K., "Three-Dimensional Flow Analysis of Turbine Balde Cascades with Leading-Edge Ejection," *Journal of Propulsion and Power*, Vol. 16, No. 1, Jan. 2000, pp. 49–56.

[6] Tyagi, M. and Acharya, S., "Large Eddy Simulation of Film Cooling Flow From an Inclined Cylindrical Jet," *Transactions of the ASME. The Journal of Turbomachinery*, Vol. 125, No. 4, Oct. 2003, pp. 734–742.

[7] Liu, K. and Pletcher, R., "Large Eddy Simulation of Discrete-Hole Film Cooling in a Flat Plate Turbulent Boundary Layer," AIAA Paper 2005–4944, June 2005, In 35th AIAA Fluid Dynamics Conference and Exhibit.

[8] Leylek, J. H. and Zerkle, R., "Discrete-Jet Film Cooling: A Comparison of Computational Results With Experiments," *Transactions of the ASME. The Journal of Turbomachinery*, Vol. 116, July 1994, pp. 358–368.

[9] Medic, G. and Durbin, P. A., "Toward Improved Film Cooling Prediction," *Transactions of the ASME. The Journal of Turbomachinery*, Vol. 124, April 2002, pp. 193–199.

[10] Pietrzyk, J. R., Bogard, D. G., and Crawford, M. E., "Hydrodynamic Measurements of Jets in Crossflow for Gas Turbine Film Cooling Applications," *Transactions of the ASME. The Journal of Turbomachinery*, Vol. 111, April 1989, pp. 139–145.

[11] Xiong, Z. and Lele, S. K., "Numerical Study of Leading Edge Heat Transfer under Free-Stream Turbulence," AIAA Paper 2001–1016, Jan. 2001, In 39th AIAA Aerospace Sciences Meeting and Exhibit.

[12] Xiong, Z., "Stagnation Point Flow and Heat Transfer under Free-Stream Turbulence," Ph.d. thesis, Aug. 2004, Deparment of Mechanical Engineering, Stanford University.

[13] Pierce, C. D., "Progress-Variable Approach for Large Eddy Simulaiton of Turbulent Combustion," Ph.d. thesis, June 2001, Deparment of Mechanical Engineering, Stanford University.

[14] Harlow, F. H. and Welch, J. E., "Numerical Calculation of Time-Dependent Viscous Incompressible Flow," *Physics of Fluids*, Vol. 8, 1965, pp. 2182–2189.

[15] Leonard, B. P., "A Stable and Accurate Convective Modelling Procedure Based on Quadratic Upstream Interpolation," *Computational Methods in Applied Mechanics and Engineering*, Vol. 19, 1979, pp. 59–98.

[16] Germano, M., Piomelli, U., Moin, P., and Cabot, W. H., "A Dynamic Subgrid-scale Eddy Viscosity Model," *Physics of Fluids, A3*, 1991, pp. 1760–1765.

[17] Iourokina, I. V. and Lele, S. K., "Towards Largy Eddy Simulation of Film-Cooling Flows on a Model Turbine Blade Leading Edge," AIAA Paper 2005–0670, Jan. 2005, In 43rd AIAA Aerospace Sciences Meeting and Exhibit.

[18] Müller, B., "Low Mach Number Asymptotics of the Navier-Stokes Equations and Numerical Implicatons," *30th Computational Fluid Dynamics*, von Karman Institute for Fluid Dynamics, Lecture Series 1999–03, March 1999, pp. 821–831.

[19] Bons, J. P., MacArthur, C. D., and Rivir, R. B., "The Effect of High Free-Stream Turbulence on Film Cooling Effectiveness," *Transactions of the ASME. The Journal of Turbomachinery*, Vol. 118, Oct. 1996, pp. 814–825.

[20] Lund, T. S., Wu, X., and Squires, K. D., "Generation of Turbulent Inflow Data for Spatially-Developing Bounday Layer Simulations," *Journal of Computational Physics*, Vol. 140, 1998, pp. 233–258.

[21] Xu, S. and Martin, M. P., "Asessment of Inflow Boundary Conditions for Compressible Turbulent Boundary Layers," *Physics of Fluids*, Vol. 16, No. 7, July 2004, pp. 2623–2639.

[22] Slotz, S. and Adams, N. A., "Large-Eddy Simulation of High-Reynolds-Number Supersonic Boundayr Layers Using the Approximate Deconvolution Model and a Rescaling and Recycling Technique," *Physics of Fluids*, Vol. 15, No. 8, Aug. 2003, pp. 2398–2412.

[23] Ferrante, A. and Eglobashi, S. E., "A Robust Method for Generating Inflow Conditions for Direct Simulations of Spatially-Develping Turbulent Boundary Layers," *Journal of Computational Physics*, Vol. 198, 2004, pp. 372–387.

[24] Durbin, P. A. and Reif, B. A. P., *Statistical Theory and Modeling for Turbulent Flows*.

[25] Spalart, P. R., "Direct Simulation of a Turbulent Boundary Layer up to $R_\theta = 1410$," *Journal of Fluid Mechanics*, Vol. 187, 1988, pp. 61–98.

[26] Cook, A. W. and Cabot, W. H., "A High-Wavenumber Viscosity for High-Resolution Numerical Methods," *Journal of Computational Physics*, Vol. 195, 2004, pp. 594–601.

[27] Cook, A. W. and Cabot, W. H., "Hyperviscosity for Shock-Trubulent Interactions," *Journal of Computational Physics*, Vol. 203, 2005, pp. 379–385.

[28] Fiorina, B. and Lele, S. K., "An Artificial Nonlinear Diffusivity Method for Supersonic Reacting Flows With Shocks," *Journal of Computational Physics, Submitted for publication*, 2005.

[29] Sinha, A. K., Bogard, D. G., and Crawford, M. E., "Film-Cooling Effectiveness Downstream of a Single Row of Holes With Variable Density Ratio," *Transactions of the ASME. The Journal of Turbomachinery*, Vol. 113, July 1991, pp. 442–449.

[30] Gopalan, R., Abraham, B. M., and Katz, J., "The Structure of a Jet in Cross Flow at Low Velocity Ratios," *Physics of Fluids*, Vol. 16, No. 6, June 2004, pp. 2067–2087.